Spatiotemporal orchestration of multicellular transcriptional programs and communications in spinal cord injury

Zeqing Wang[1,5,6], Zhuxia Li[2,5,6], Tianle Luan[1,5], Guizhong Cui[4], Shunpan Shu[1,5], Yiyao Liang[3], Kai Zhang[1,5], Wei Yu[3], Jihong Cui[1], Ang Li[3,4,*], Guangdun Peng[2,4,5,*], and Yanshan Fang[1,5,*]

[1]Interdisciplinary Research Center on Biology and Chemistry, Shanghai Institute of Organic Chemistry, Chinese Academy of Sciences, Shanghai, 201210, China

[2]Center for Cell Lineage and Development, CAS Key Laboratory of Regenerative Biology, Guangdong Provincial Key Laboratory of Stem Cell and Regenerative Medicine, GIBH-HKU Guangdong-Hong Kong Stem Cell and Regenerative Medicine Research Centre, Guangzhou Institutes of Biomedicine and Health, Chinese Academy of Sciences, Guangzhou, 510530, China

[3]Guangdong-Hong Kong-Macau Institute of CNS Regeneration, Key Laboratory of CNS Regeneration of Ministry of Education, Jinan University, Guangzhou, 510632, China

[4]Bioland Laboratory (Guangzhou Regenerative Medicine and Health Guangdong Laboratory), Guangzhou, 510005, China

[5]University of Chinese Academy of Sciences, Beijing, 100049, China

[6]These authors contributed equally to this work

***Co-corresponding authors**:

Ang Li: anglijnu@jnu.edu.cn

Guangdun Peng: peng_guangdun@gibh.ac.cn

Yanshan Fang: fangys@sioc.ac.cn

Running title: Spatial transcriptomics of SCI

Keywords: RNA-seq, spatial transcriptomics, spinal cord injury, astrocyte, neuroinflammation, neuroprotection.

Word counts: ~7,450 words (*excluding the title page, acknowledgements and references)*

ABSTRACT (*≤200 words*):

The spinal cord is an assembly of spatially organized multicomponent cells that coordinates the transmission of motor, sensory and autonomic nerve functions. Although complex pathological and cellular alterations in spinal cord injury (SCI) have been documented, the spatiotemporal architecture of the molecular events that drive the injury progression remains poorly understood. Here, we conducted a spatially resolved transcriptomic profiling of gene expression in a mouse model of SCI, which demonstrated the comprehensive gene co-expression networks and transcriptional programs underlying the anatomic disorganization induced by SCI. Further, with integration of the single-cell RNA-sequencing datasets, we delineated the exquisite orchestration of multicellular transcriptional programs and *in situ* cell-cell interactions following SCI, and discerned regional diversity of astrocyte populations in intact and injured spinal tissues. The spatial molecular features endow the cell types with new biological significance, showcased by the identification of a distinct, SCI-induced population of astrocytes that exhibit functional heterogeneity in promoting both beneficial neuro/synapto-supportive and deleterious pro-inflammatory programs. Together, our dataset and analysis provide a rich resource and a spatiotemporal molecular atlas that potentially disentangle the cell organization in mammalian SCI and advance the injury management.

42 **MAIN** (*≤2,500 words*):

43 Spinal cord injury (SCI) can cause permanent motor, sensory and/or autonomic dysfunctions,
44 accompanied by various local or systemic complications. Multiple intertangled cascades of
45 cellular and molecular events take place in the injured spinal cord, such as neuronal and axonal
46 degeneration, neuroinflammation and neuroimmune activation, glial scar formation, and
47 demyelination. Both the primary insult and the secondary responses contribute to the pathological
48 changes and the overall prognosis (Ahuja et al., 2017; Anjum et al., 2020; Zhang et al., 2021).
49 With the advent of the RNA-sequencing (RNA-seq) technology especially single-cell (sc) and
50 single-nucleus (sn) RNA-seq, valuable insights into the transcriptional alterations and cell type-
51 specific regulatory programs in SCI have been gained (Noristani et al., 2016; Wang et al., 2021;
52 Milich et al., 2021). However, the spinal cord is a spatially organized organ and the information of
53 the molecular anatomy of these post-SCI changes and their *in situ* cell properties are largely
54 missing.

55 A spatially resolved view of the changes in the transcriptional landscapes may enable
56 identification of unknown regulatory mechanisms and facilitate the development of new strategies
57 for treating human diseases. Indeed, the recent innovation in spatial transcriptomics, which allows
58 high-throughput measurement of gene expression while retaining the anatomic information (Moor
59 and Itzkovitz, 2017; Williams et al., 2022), has been applied to profile cell atlases and characterize
60 different biological processes, including normal tissue and organ development, pathological and
61 neurodegenerative diseases (Asp et al., 2019; Maniatis et al., 2019; Peng et al., 2019; Chen et
62 al., 2020; Ortiz et al., 2020; Fawkner-Corbett et al., 2021; Rao et al., 2021; Li and Peng, 2021;
63 Ratz et al., 2022; Tavares-Ferreira et al., 2022). Given its value in molecular profiling of physically
64 intact tissue samples in chronic conditions, here we made an attempt to employ spatial
65 transcriptomics to investigate mechanically damaged mouse spinal tissues in acute injury, aiming

66 to gain a holistic understanding of the transcriptional programs underlying the SCI-induced
67 molecular and cellular changes in their morphological context.
68

69 **The mouse SCI model and the workflow of the spatial transcriptomic analyses**

70 For the spatial transcriptomic analysis of mammalian SCI in this study, the spinal cord of
71 C57BL/6J mice was fully transected at the tenth thoracic vertebra (T10) (Fig. 1a and Extended
72 Data Fig. 1a). The motor function and the morphology of the spinal cord after injury were
73 examined at 0 (sham), 3, 24 and 72 hours post injury (hpi) to confirm a complete transection
74 (Extended Data Fig. 1b-d). We performed hematoxylin and eosin (H&E) staining on transverse
75 sections of various distances from the lesion center on both the rostral (-) and caudal (+) segments
76 (Extended Data Fig. 1e). As shown in Extended Data Fig. 1d and e, the spinal cords were severely
77 deformed within ±0.25 mm, precluding an informative spatial transcriptomic analysis. Therefore,
78 the rostral (-) and the caudal (+) sections at ±0.5 and ±1.0 mm from the injury site were subjected
79 to the 10x Visium spatial RNA-seq analysis. Four consecutive cryo-sections each at ±0.5 and
80 ±1.0 mm were captured, and the spinal sections of the same distance at different time points (0,
81 3, 24 and 72 hpi) were attached to the same Visium Gene Expression slide and processed
82 simultaneously in the subsequent procedure (Fig. 1b). Together, 64 spinal cord sections from 9
83 different mice were examined in this spatial transcriptomic analysis, representing an inclusive
84 coverage of the dynamic injury responses in a high spatial and temporal resolution.

85 Overall, 22,820 spatial spots were obtained and profiled after filtering, with a mean of 12,574
86 RNA reads and 3,990 genes per spot (Extended Data Fig. 2a-d and Supplementary Table 1). The
87 discernible grey matter (GM) regions containing condensed neuronal cells showed higher
88 numbers of expressed genes (Extended Data Fig. 2d). We compared the intra- and inter-
89 correlations of the sample groups and found a high data reproducibility of the replicate sections
90 within each group at the bulk level (Extended Data Fig. 2e). We therefore analyzed all the sampled

spots of the four replicates but visualized the results on each representative sample section in all the spatial view charts in this study.

Further spatiotemporal evaluation of the expression of known injury-related genes (e.g., *Atf3*, *Hmox1* and *Timp1*), aka, the injury score (see Methods), displayed remarkable patterns in association with the injury time, the distance and the anatomy of the spinal cord (Extended Data Fig. 2f). For example, the ±0.5 mm spinal sections at 72 hpi displayed the highest injury scores (Extended Data Fig. 2f, g) and the lowest transcriptomic similarity to others (Extended Data Fig. 2e), which were in accordance with the most severe damage among all the 64 sections (Extended Data Fig. 1e). Therefore, in the subsequent data analyses, we focused on revealing: (1) the spatiotemporal molecular annotation of the spinal cord anatomy, (2) the gene co-expression modules and regulatory networks, and (3) the cell type composition and cell-cell communications in response to SCI (Fig. 1c). For readers with broader research interests, an interactive data exploration portal is available at (*the website will be accessible to the public upon the acceptance of the manuscript*).

Cluster analysis of the spatial spots reveals anatomic domain- and injury time-featured expression profiles of SCI

First, we performed dimension reduction and cluster visualization on the collective spatial spots using uniform manifold approximation and projection (UMAP) (see Methods). Seven distinct gene expression clusters were identified (Fig. 1d) and Clusters 1, 2, 6 and 7 showed a bona fide anatomic and molecular annotation of the intact spinal cord at 0 and 3 hpi (Fig. 1e). This allowed us to categorize the seven clusters into four major anatomic regions: white matter (WM), middle grey (MG), dorsal horn (DH) and ventral horn (VH) (Fig. 1f). With the injury score increased along the time (Extended Data Fig. 2f, g), the boundary of the anatomic regions became less clear (Fig. 1e). However, the spatiotemporal clusters could still be classified to the four major spatial domains of the spinal cord following the coherence in the UMAP plot (Fig. 1g), which showcased the

advantage of spatial transcriptomics in providing the molecular annotation of tissue architecture to better understand the SCI pathology.

Like the spatial domain, the major transcriptomic difference could be attributed to the time after injury (Fig. 1h). In contrast, the rostral/caudal directionality and the distance to the injury site showed minimal impacts on distinguishing the spatiotemporal clusters (Fig. 1i, j). Consistently, analysis of differentially expressed genes (DEGs) revealed remarkable domain-dependent alterations, whereas only a small number of directionality- or distance-specific DEGs were identified during SCI (except for the ±0.5 mm sections at 72 hpi, where more severe damage was associated) (Extended Data Fig. 3a-c). As such, we focused on the factors of spatial domain and injury time in the subsequent analyses (also see Extended Data Fig. 3d-g).

A remarkable shift of the compositions of spatiotemporal clusters in the WM and MG domains was elicited by SCI (Fig. 1k). To understand the molecular changes and functional relevance of these changes, we identified the cluster-enriched genes (CEGs) for each cluster and analyzed their spatiotemporal expression profiles (Fig. 1l). The CEGs included not only the well-known markers of the four anatomic domains of the intact spinal cord, such as *Mbp* (Cluster 1) for WM, *Snap25* (Cluster 2) for MG, *Tac2* (Cluster 6) for DH and *Prph* (Cluster 7) for VH, with their spatial expression validated by *in situ* hybridization (ISH) (Fig. 1m), but also uncharted signature genes for injured spatial domains (Extended Data Fig. 4). Gene ontology (GO) term enrichment analyses of the CEGs revealed the biological processes that not only reflect the unique physiological function of the different anatomic regions, but also underlie the pathological progression of SCI. For example, Cluster 1 was predominantly localized to the WM at 0 and 3 hpi (Fig. 1k), and its CEGs, such as the myelin-related genes *Plp1*, *Mog* and *Mbp* (Monje, 2018), were enriched in the biological functions of myelination and oligodendrocyte differentiation (Fig. 1l). At 24 and 72 hpi, the main clusters of the WM switched to Clusters 4 and 5 (Fig. 1k), whose CEGs, such as the reactive astrocyte markers *Vim* and *Tm4sf1* (Li et al., 2022a) in Cluster 4 and the activated macrophages markers *Lyz2* and *Lgals3* (Willemsen and Winther, 2020) in Cluster 5, were

143 enriched with the terms of protein synthesis, cell migration, responses to wounding, *etc*. (Fig. 1l).
144 Thus, the switch of the spatiotemporal clusters in the WM between 3 and 24 hpi suggested that
145 a reduction of myelination-related functions along with the activation of astrocytes and infiltration
146 of myeloid cells took place in the WM in the subacute phase during SCI.
147

148 **Spatiotemporal analysis of gene co-expression patterns and transcriptional programs in**
149 **SCI**

150 Next, to depict the intricate and dynamic transcriptional changes in SCI and unveil the
151 commonalities in the molecular events and regulations, we performed the weighted gene co-
152 expression network analysis (WGCNA, Langfelder and Horvath, 2008) (Fig. 2a). Thirty-three
153 spatially and temporally co-expressed gene modules (CGMs) were identified (see Methods and
154 Supplemental Table 2) and they displayed unique and diverse spatiotemporal expression patterns
155 (Extended Data Fig. 5a-c), providing an unbiased molecular annotation of the injury-induced
156 responses in SCI. We further performed module enrichment with the anatomic domains and
157 identified spatial domain- and injury time-dependent module activities (Fig. 2b). For example,
158 CGM13 showed an injury-induced expression in the WM specifically at 3 hpi, after which the
159 expression was sharply decreased (Fig. 2c). This module was highly associated with the cellular
160 functions of regulating the ERK1/2 signaling cascade and the node genes of the connectivity
161 network, *Csrnp1* and *Maff*, were known players in stress-induced immune and inflammatory
162 responses (Bensellam et al., 2015; Macdonald et al., 2018) (Fig. 2c). Thus, CGM13 likely
163 represented a group of MAPK/ERK-mediated “early response genes” regulating immunity and
164 inflammation in the acute phase of SCI.

165 In addition, we noticed that some modules, such as CGM9 and CGM11, exhibited an
166 interesting spatiotemporally-complementary expression pattern: CGM9 was expressed at a low
167 level in the WM of the intact spinal cord (0 hpi) and at 3 hpi, but was robustly increased at 24 hpi,
168 which expanded into the MG in the ±0.5 mm sections at 72 hpi (Fig. 2d). In contrast, CGM11 was

169 highly expressed in the MG at 0 and 3 hpi, which started to decrease at 24 hpi and only retained
170 weak expression at 72 hpi, with the expression in the ±0.5 mm sections reduced the most (Fig.
171 2e). Scrutinizing the biological functions and the connectivity network of the genes enriched in
172 these two CGMs, we found that CGM9 was mainly involved in stress, injury and immune
173 responses with the node genes such as *Ecm1* (encoding an extracellular and structural protein
174 contributing to the maintenance of tissue integrity and homeostasis) and *Emp3* (encoding a
175 transmembrane protein mediating cell proliferation and cell-cell interactions) (Fig. 2d); whereas
176 CGM11 was mostly associated with the function and regulation of neuronal synapse with the node
177 genes such as *Rab3a* (encoding a GTPase involved in vesicle exocytosis and plasm membrane
178 repair) and *Mdh1* (encoding a cytosolic isozyme in the citric acid cycle) (Fig. 2e). Thus, the
179 complementary spatiotemporal expression pattern of the two CGMs underscored the interplay of
180 SCI-induced immune activation and inflammation with the neuronal loss and dysfunction during
181 SCI. (A full characterization and analysis of the other CGMs, including the spatiotemporal
182 expression pattern in response to SCI, the connectivity network, the GO term enrichment and the
183 top 3 upstream regulatory transcription factors (TFs) for each CGM, were shown in Extended
184 Data Fig. 5 and 6a, b).

185 To further unravel the regulatory mechanisms that determine the spatiotemporal changes in
186 gene expression in SCI, we performed single-cell regulatory network inference and clustering
187 (SCENIC) analysis (Aibar et al., 2017) to analyze transcription regulons that are turned on or off
188 in response to SCI. Overall, 147 regulons were identified and classified into seven co-expressed
189 regulon modules (RMs) (Fig. 2f and Supplemental Table 3). The RMs showed distinct anatomic
190 region- and injury time-specificity (Fig. 2g) as well as diverse spatiotemporal patterns (Fig. 2h and
191 Extended Data Fig. 6c-h). Taking the WM as an example, RM2 was the main RM at 0 and 3 hpi
192 (Fig. 2g, h), which was superseded by RM3 at 3 and 24 hpi (Fig. 2g and Extended Data Fig. 6d)
193 and finally by RM1 at 72 hpi (Fig. 2g and Extended Data Fig. 6c). Along with the change of the
194 RMs, the main regulons in the WM switched from those represented by the TFs of Sox10, Oligo2

195 and Srebf2 (RM2), to Fos, Jun and Nfkb1/2 (RM3), and ultimately to Stat3, Stat6 and Irf5 (RM1)
196 (Fig. 2i). Sox10 and Oligo2 are important TFs in oligodendrocyte differentiation and maturation
197 (Zhou et al., 2000), and Srebf2 regulates genes involved in cholesterol biosynthesis (Pierrot,
198 2011); Fos and Jun are key TFs in TGFβ-mediated signaling and regulate cell proliferation,
199 differentiation and death (Shaulian and Karin, 2001), and Nfkb1/2 is a central activator of genes
200 related to inflammation and immune functions (Liu et al., 2017); and Stat3, Stat6 and Irf5 mediate
201 gene expression in response to cell stimuli and regulate cell growth and apoptosis (Yan et al.,
202 2016). Together, the switch of the main RMs in the WM (Fig. 2g) was in agreement with the
203 changes of the spatiotemporal clusters in the WM during SCI (Fig. 1k), which might drive the
204 injury-induced dysfunction of oligodendrocytes and dysregulation of lipid metabolism as well as
205 the activation of inflammation and cytokine activity in the WM. Of note, RM1 was present in other
206 spatial domains in addition to the WM at 72 hpi (Extended Data Fig. 6c), suggesting a widespread
207 upregulation of inflammatory genes in the spinal cord at this time point. Nevertheless, we noticed
208 that the RMs enriched in the WM were mostly anti-correlated with those enriched in the MG,
209 indicating that the main anatomic identity of the spinal cord was maintained at the transcription
210 regulon level during SCI.
211

212 **Integration of the SCI scRNA-seq data for an *in situ* multicellular gene expression and cell**
213 **communication atlas**

214 Because the Visium spot is not single-cell resolution, to allocate the cell type information to the
215 SCI spatial spots in a comparable manner, we performed deconvolution analysis by robust cell
216 type decomposition (RCTD) (Cable et al., 2022b; also see Methods) based on one normal and
217 one injured spinal cord scRNA-seq datasets (Rosenberg et al., 2018; Milich et al., 2021). The
218 proportions of different cell types detected within a single spatial spot were displayed as a pie
219 chart and the entire spinal cord section was displayed as an assembly of the spatial pie charts
220 (Fig. 3a and Extended Data Fig. 7a). We found the overall composition of the main cell types and

221 their anatomic localizations were in good accordance with the spatial architecture of the spinal
222 cord. For example, neurons and oligodendrocytes were predominantly localized to the GM and
223 the WM, respectively (Fig. 3b). Interestingly, we found that the two molecularly-defined astrocyte
224 subtypes, astrocyte-*Gfap* and astrocyte-*Slc7a10* (Rosenberg et al., 2018), showed distinct and
225 mutually exclusive distributions in the white (namely, astrocyte-WM) and grey matter (namely,
226 astrocyte-GM), respectively (Fig. 3b), which represented the general categories of astrocyte
227 heterogeneity in location of white (fibrous astrocyte) versus grey matter (protoplasmic astrocyte)
228 (Molofsky et al., 2012).

229 Upon injury, the cell type composition in the spinal cord demonstrated the spatial domain-
230 and the injury time-associated alterations (Fig. 3c and Extended Data Fig. 7b, c). For example,
231 both neurons in the GM and oligodendrocytes in the WM decreased slightly at 24 hpi and
232 drastically at 72 hpi (Extended Data Fig. 8a, b), indicative of injury-induced neurodegeneration
233 and demyelination. Homeostatic microglia were substantially reduced at 3 hpi (Extended Data Fig.
234 8c), whereas reactive microglia emerged at 24 and 72 hpi (Extended Data Fig. 8d).
235 Oligodendrocyte precursor cells (OPCs) were increased along the time after SCI (Extended Data
236 Fig. 8e), which might represent a compensatory myelinogenesis response to injury. Several
237 peripheral immune and inflammatory cell types including myeloid cells, macrophages, monocytes
238 and neutrophils were induced, which showed up in the injured spinal cord at various time points
239 after SCI (Extended Data Fig. 8f-i). Meanwhile, fibroblasts, ependymal cells and vascular cells
240 previously shown to participate in the scar formation (Soderblom et al., 2013; Meletis et al., 2008;
241 Lacroix et al., 2014) were dramatically activated by SCI (Extended Data Fig. 8j-l). Noteworthily,
242 our analysis allocated ependymal cells only in one or two spatial spots at the very center of the
243 uninjured spinal cord, which faithfully reflected the anatomic localization and function of
244 ependymal cells in lining the central canal of the spinal cord, and developed a diverse
245 astroependymal distribution later in SCI (Extended Data Fig. 8k). Hence, deciphering *in situ* cell

246 type compositions and their spatiotemporal dynamics during SCI provided a reliable source for
247 characterizing SCI-induced cellular responses and interactions.

248 Cell-cell interaction plays important roles in maintaining tissue integrity and function. To
249 denote confident *in-situ* cell-cell interactions from our spatial transcriptomic data, we performed a
250 spatial-aware cell-cell communication analysis (SA-CCC). In brief, spatial colocalization of cell-
251 type pairs within spots and spot-enriched ligand_receptor (L_R) pairs deduced from CellChat
252 package (Jin et al., 2021) were subjected to co-occurrence test (Fig. 3d; also see Methods). Upon
253 injury, both the number of interacting L_R pairs per cell-type pair and the complexity of the network
254 of co-localized cell types were markedly increased, especially at 72 hpi (Fig. 3e), indicating much
255 escalated diversity of cell communications induced by SCI. Among all the cell types,
256 oligodendrocytes, astrocytes and neurons had the most extensive connections and served as the
257 nodes to interact with other cell types in the intact spinal cord and within 24 hpi. At 72 hpi, while
258 oligodendrocytes and astrocytes remained as the nodes of the cell-cell interactions, the
259 connectivity of macrophages, microglia, OPCs and fibroblasts were substantially increased,
260 suggesting that the latter become the cell communication coordinators in the subacute phase of
261 SCI.

262 To pinpoint the specific L_R pairs that regulate the spatiotemporal dynamics of cell-cell
263 communications, we selected the top L_R pairs in each cell-type pair and categorized them into
264 three main classes: (Class-I) the expression of the L_R pairs increased or emerged upon injury
265 (e.g., the *Col_Sdc* families); (Class-II) the expression of the L_R pairs switched from one cell-type
266 pair to another (e.g., the *Nrxn_Nlgn* families); and (Class-III) the expression of the L_R pairs
267 decreased or disappeared (e.g., the *Fgf_Fgfr* signaling pathway) (Fig. 3f). Further investigation
268 revealed that Class-I L_R pairs mainly participated in cell matrix adhesion, cell migration, immune,
269 angiogenesis and wound healing; Class-II L_R pairs were involved in neuron and synapse
270 adhesion, dendritogenesis, actin remodeling, and neuroprotection. Class-III L_R pairs functioned

271 in regulating axon growth and guidance, dendritic spine development, synapse formation and
272 elimination, and myelination (Fig. 3g).

273 Compared to the cell-cell communication analysis based solely on scRNA-seq datasets, the
274 SA-CCC analysis here is featured by identifying both the expression levels and the *in situ*
275 interacting cell types for a particular L_R pair in a context-dependent manner. For example, the
276 L_R pair of *Spp1_Cd44* was expressed predominantly in the WM at moderate levels at 0 and 3
277 hpi, which was increased remarkably at 24 hpi (primarily in the WM and scattered in some GM
278 regions) and spread throughout the entire spinal cord section at 72 hpi (Fig. 3h). Accompanying
279 the profound induction of the *Spp1_Cd44* pair expression, the interactions of which cell-type pair(s)
280 this L_R pair mediated expanded from "oligodendrocyte_astrocyte-WM" to "astrocyte-WM_OPC"
281 in the WM at 24 hpi and finally to "oligodendrocyte_macrophage" and "OPC_macrophage"
282 massively in the GM at 72 hpi (Fig. 3f, h), suggesting a multifaceted role of this L_R pair in different
283 phases of SCI.

284

285 **Injury induces redistribution and repurposing of astrocytes-WM into the GM of the spinal**
286 **cord**

287 Astrocytes are morphologically and functionally diverse and play vital roles in the nervous system
288 in both physiological and pathological conditions (Escartin et al., 2021). Being a significant portion
289 in the spinal cord, although total astrocytes only slightly increased during SCI, the proportions of
290 the two astrocyte subtypes altered dramatically (Fig. 3c). In fact, astrocytes-WM and astrocytes-
291 GM displayed quite different spatiotemporal distribution changes in response to SCI: astrocytes-
292 WM were largely unchanged at 3 hpi but were drastically increased at 24 and 72 hpi, at which
293 they were even present in the GM region; astrocytes-GM were increased at 3 hpi but then
294 drastically decreased at 24 hpi and became almost undetectable at 72 hpi (Fig. 4a, c). In order to
295 understand the molecular basis of the difference in the physiological functions and injury

296 responses of the two subtypes of astrocytes, we performed a series of exploratory data analyses
297 and also cross-tested with the published scRNA-seq datasets of mouse SCI (Fig. 4e).

298 First, we examined the gene expression features of the deconvoluted astrocytes-WM and -
299 GM in the uninjured spinal cord (0 hpi) when they were spatially distinct. Forty-seven DEGs were
300 identified by cell type-specific inference of differential expression (C-SIDE; Cable et al., 2022a;
301 also see Methods) (Extended Data Fig. 9a). GO term analysis of the DEGs and their upstream
302 transcription regulons (Extended Data Fig. 9b, c) pointed to the molecular basis underlying the
303 functional divergences of these two subtypes: astrocytes-WM were highly associated with the
304 function of gliogenesis, glial cell development and differentiation, inhibition of neuronal apoptosis
305 and wound response, with the TFs of the main regulons (e.g., Jund, Sox9, Atf3 and Irf8) enriched
306 in cell proliferation, differentiation and death, and cellular stress and immune responses (Yáñez
307 and Goodridge, 2016; Sykes et al., 2018; Molofsky et al., 2013); astrocytes-GM were energetically
308 active and provided trophic supports to neurons by mediating transmembrane transport of ion,
309 metabolites and neurotransmitter, with the TFs of the main regulons (e.g., Esrra and Esrrg)
310 enriched in cellular energy production (Saul et al., 2017; Frattini et al., 2018). Therefore, our
311 spatial classification of astrocytes-WM and astrocytes-GM corroborates the different physiological
312 functions of the known astrocyte subtypes in the mammalian nervous system (Sidoryk-
313 Wegrzynowicz et al., 2011).

314 Next, we re-analyzed the astrocytes in the scRNA-seq study of mouse SCI (Milich et al.,
315 2021). UMAP clustering also separated injured astrocyte cells into two distinct clusters at the
316 molecular level, which were denoted as astrocytes-WM and astrocytes-GM by their shared
317 signature genes with related spatial spots (e.g., *Gfap* and *Dhrs1* for astrocytes-WM and *Pla2g7*
318 and *Slc7a10* for astrocytes-GM; Extended Data Fig. 9d, e). We validated the subtype-specific
319 changes by examining the spatiotemporal expression patterns of the representative marker genes
320 of these two spatially-defined astrocytes (*Gfap* and *Pla2g7*) in the intact and injured spinal cords
321 by ISH (Fig. 4b, d). To further confirm this injury-induced cellular change at the protein level, we

322 performed immunostaining of the spinal astrocytes with anti-GFAP. The results not only verified
323 the predominant localization and fibrous appearance of $GFAP^+$-astrocytes in the WM of the
324 uninjured spinal cord but also showed a remarkable emergence of $GFAP^+$-astrocytes in the GM
325 after injury, and these GM-relocated $GFAP^+$-astrocytes displayed a hypertrophic morphology
326 (Extended Data Fig. 9f).

327 The loss of astrocytes-GM at 24 and 72 hpi and the striking occupation of astrocytes-WM in
328 the GM prompted us to examine the possible role of GM-relocated astrocytes. By analyzing the
329 astrocyte-neuron interactions in the GM region, we revealed a clear switch of neuron-interacting
330 astrocytes from “astrocytes-GM” to “astrocytes-WM” in the GM after injury (Fig. 4f), accompanied
331 by the switch of the spatial L_R pair of *Nrxn3_Nlgn3* following the interacting cell-type pairs. The
332 *Nrxn3_Nlgn3* is well-known for mediating astrocyte-neuron interaction and regulating astrocyte
333 maturation as well as synapse formation and function (Stogsdill et al., 2017). These findings
334 strongly suggested a functional relay of the original astrocytes-GM to the GM-relocated
335 astrocytes-WM in the interaction with neurons in the GM after SCI.

336 To avoid confusion due to the discrepancy in the anatomic localization and the transcriptional
337 features, we designated the injury-induced, GM-relocated astrocytes as astrocytes-GMii. To
338 address the question whether these astrocytes-GMii originated from local cell division or remote
339 cell migration, we calculated and compared the proliferation score and the migration score at the
340 section level (Fig. 4g and see Methods) and for each cell type (Extended Data Fig. 9g-i). The
341 results showed that significant cell proliferation was detected in astrocytes-WM, reactive microglia
342 and other cell types only at 72 hpi (Fig. 4g and Extended Data Fig. 9g, i), much later than the time
343 when a large number of astrocytes-GMii emerged (Fig. 4a). In contrast, the migration score
344 started to increase in astrocytes-WM as early as 3 hpi, which kept rising and expanded into the
345 GM at 72 hpi (Fig. 4h and Extended Data Fig. 9h). Notably, astrocytes-GM persistently showed
346 the low proliferation and migration scores with a minimal increase of migration at 3 hpi (Extended
347 Data Fig. 9g, h). In addition, our analysis of the SCI scRNA-seq dataset (Milich et al., 2021) also

348 indicated a markedly higher migration ability associated with astrocytes-WM than astrocytes-GM
349 (Extended Data Fig. 9j). Taken together, astrocytes-GMii likely originated from astrocytes-WM,
350 which migrated into the GM at the early phases of SCI and proliferated to replenish for the loss of
351 original astrocytes-GM at the later phases.
352

353 **The astrocytes-GMii are molecularly distinct from the original astrocytes-WM/-GM and**
354 **exhibit a diverse range of functional heterogeneity**

355 We were keen to know what unique molecular features astrocytes-GMii possess that made them
356 distinct from the other astrocytes-WM and drove them into the GM in response to SCI. To this
357 end, we subjected all astrocytes-WM-containing spots in our spatial transcriptomic data to a
358 pseudotime analysis (see Methods). To exclude potential confounding influences from other cell
359 types in the same spot, only the 317 marker genes used to define astrocytes in the SCI scRNA-
360 seq deconvolution (Milich et al., 2021) were included. Despite considerable overlapping in their
361 expression patterns, these 317 marker genes could be clustered into 4 spatiotemporally-separate
362 astrocyte (SA) gene groups (Fig. 4i and Supplemental Table 4). Among them, the SA-1 group
363 showed specifically high expression in the GM at 24 and 72 hpi, while the SA-4 group also showed
364 increased expression in the injured GM, although to a lesser extent (Fig. 4i), which together might
365 spatially define the astrocyte-GMii features. To assess whether these proposed astrocyte-GMii
366 signature genes could distinguish astrocytes-GMii from other astrocytes-WM, we re-clustered the
367 astrocytes in the single-cell study (Milich et al., 2021). Indeed, the *Gfap*-positive single-cell
368 astrocytes were gated into two distinct populations based on the SA-1 and SA-4 gene sets,
369 astrocytes-GMii and the rest astrocytes-WM (Extended Data Fig. 9k), which were well separated
370 from each other in the UMAP analysis, with one significantly presenting the GM spatial features
371 and the other showing the WM (Fig. 4j).

372 To facilitate the precise sorting of injured astrocytes, we expand the spatially-defined
373 molecular features of astrocytes-GMii by identifying signature genes in the whole single-cell

374 dataset based on the aforementioned classifications. We also examined the surface markers, and
375 the upstream TFs of these different astrocyte populations (Extended Data Fig. 9l-n). It was worth
376 noting that astrocytes-GMii were strongly associated with the increased activity of the Irf and Stat
377 families of TFs, pointing to the immune-triggered transition of astrocytes-WM to astrocytes-GMii.
378 All together, these findings based on the expanded signature genes demonstrated that our
379 spatiotemporal transcriptomic analysis could provide valuable metrics to annotate independent
380 cell states that are often hidden to common single-cell approaches.

381 In order to further understand the molecular reprogramming underlying the transition of
382 astrocytes-WM to astrocytes-GMii, we performed pseudo-trajectory analysis by slingshot (Street
383 et al., 2018) in the SCI single-cell dataset. We identified continuous transitive structures between
384 associated clusters in the low dimensional data (Fig. 4k) and highlighted the most dramatically
385 upregulated genes during this transition (Fig. 4l). One of such genes was *Igfbp2* (insulin-like
386 growth factor binding protein 2) and we performed fluorescence ISH (FISH) of *Igfbp2* together
387 with immunostaining of GFAP to confirm that astrocytes-GMii, represented by the *Igfbp2*$^+$-GFAP$^+$
388 double-positive cells, were specifically induced in the GM of injured spinal cord especially at 72
389 hpi (Fig. 4m). Of note, the GFAP$^+$ signal displayed a pattern invading from the WM into the GM,
390 which again indicated the WM-origin of astrocytes-GMii. The *Igfbp2*$^+$ signal appeared to emerge
391 within the GM and was drastically increased at 72 hpi, suggesting that the transition to astrocytes-
392 GMii occurred after astrocytes-WM had arrived in the GM.

393 To explicate the biological significance of this switch, we compared the DEGs of the three
394 populations of astrocytes-WM, -GM and -GMii in our spatial transcriptomic data (Supplemental
395 Table 5). Astrocytes-GMii appeared to share several neurotrophic functions in common with
396 astrocytes-GM (Fig. 4n), suggesting a functional replacement of astrocytes-GM by astrocytes-
397 GMii. In addition, the astrocyte-GMii signature genes such as *Vegfa*, *Gpr37l1*, *Fgfr3* and *Fgfr1*
398 were associated with a protective role in neurological disorders (Kaufmann et al., 2022). Finally,
399 re-analysis of the astrocytes-*Gfap*$^+$ in the SCI scRNA-seq dataset (Milich et al., 2021) by sub-

400 clustering (Fig. 4o) using the astrocyte-GMii spatial features (see Methods and Supplemental
401 Table 6) identified 3 sub-clusters of astrocytes with high astrocyte-GMii scores (Fig. 4p). The DEG
402 and GO term analyses indicated that these three sub-clusters were each enriched in the functions
403 of RNA splicing and processing, cell migration, and immune response and sterol biosynthesis,
404 respectively (Fig. 4q). Thus, the astrocytes-GMii were not a homogeneous population but rather
405 represented a diversity of injury-induced, WM-originated, GM-relocated sub-groups of astrocytes,
406 and they were thereby able to simultaneously execute the seemingly contradictory roles of both
407 pro-inflammatory and neurotropic functions in SCI. Future investigation is warranted for the finer
408 classification of the astrocytes-GMii and understanding of their spatial features and functional
409 implications.

410 **Discussion**

411 The spinal cord is a highly structured organ composed of various cell types that are well organized
412 to perform complicated yet interdependent physiological functions. Two earlier spatial
413 transcriptomic studies of the mammalian spinal cord identified pathway dynamics during the
414 disease progression of ALS (Maniatis et al., 2019) and described various cell transcriptional states
415 over the course of injury-induced scar formation (Gong et al., 2022). Meanwhile, several snRNA-
416 and scRNA-seq studies have demonstrated complex cellular heterogeneity and interactions in the
417 mouse spinal cord (Rosenberg et al., 2018; Sathyamurthy et al., 2018; Zeisel et al., 2018; Milich
418 et al., 2021; Li et al., 2022b; Matson et al., 2022). Thus, how the diverse cell types respond and
419 cross-talk to one another in a spatial- and context-dependent manner in the early phases of SCI
420 is central to the understanding of the molecular events that drive the pathological process and yet
421 remain incompletely understood. Here, we implemented the spatial transcriptomic analysis of a
422 time serial of transverse spinal cord sections in the acute and subacute phases of SCI. We
423 characterized and analyzed the spatiotemporal changes in gene expression, TF activities, regulon
424 networks, cell compositions as well as cell-cell communications in SCI. To demonstrate the utility
425 of the rich information generated in this study, we have set up an interactive web-portal for other
426 researchers to explore *in situ* gene expression dynamics in SCI (*the website will be accessible to*
427 *the public upon the acceptance of the manuscript*).

428 Anatomic heterogeneity in gene expression revealed by the spatial transcriptomic analysis in
429 this study allowed the identification of four molecularly-defined, spatially-distinct domains of the
430 spinal cord, and a large number of domain-enriched signature genes were uncovered in finer
431 details. Interestingly, we found that the WM responded to injury more robustly and sophisticatedly
432 than the GM, as the main molecular features of the WM shifted twice from Cluster 1 to 4 and to
433 5, whereas the GM changed only once from Cluster 2 to 3 (Fig. 1). Further, the WM appeared to
434 respond earlier than the GM, evidenced by the fast activation of the early response gene modules

435 (e.g., CGM13 and CGM22) in the WM but not GM at 3 hpi, whose cellular functions were enriched
436 in the MAPK/ERK signaling cascade, cytokine production and other immune and inflammatory
437 responses (Fig. 2). Thus, the WM is not a “passive” tissue that merely insulates the GM and
438 responds secondarily to neuronal damage. Rather, the WM and the cell types within it behave as
439 the "first responders” and play a more active, primary and probably deciding role in SCI than we
440 thought.

441 SCI triggers multicellular gene expression changes in a temporally and spatially coordinated
442 manner. By combining with scRNA-seq data, we illustrated a systematic overview of *in situ* cell
443 responses during SCI, which is more authentic and reliable compared with the single-cell data
444 that are limited by the sampling bias in the tissue dissociation procedure and low-coverage
445 sequencing (Denisenko et al., 2020). Besides, the cell communication based on the single-cell
446 data lacks the actual spatial constraint so that the calculated “interacting cells” may localize far
447 apart and a large portion of the speculated cell-cell interactions cannot occur in physiological
448 context. To amend this, we took the advantage of the spatial transcriptomics and developed a
449 new computation strategy (SA-CCC) to unfold the cell communication by simultaneous evaluation
450 of the physical distance between any cell-type pair and the locally aggregated expression level of
451 a L_R pair that is supposed to express in this cell-type pair (Fig. 3). Thus, our spatial
452 transcriptomic analysis not only identifies distinct categories of cell-cell interactions that were
453 rigorously restricted to spatial domain or injury time in SCI, but also provides a useful toolset (*will*
454 *be available to the public upon the acceptance of the manuscript*) to evaluate cell-cell
455 communications in the comprehensive multicellular context in biological processes and diseases.

456 The interregional and intraregional heterogeneity of astrocytes is widely recognized in both
457 the brain and spinal cord (Yoon et al., 2017; Hasel et al., 2021). Different subtypes of astrocytes
458 display distinct morphologies, physical functions and gene expression patterns, and the
459 heterogeneity is closely related with the local environment. By leveraging the spatiotemporal
460 transcriptomic allocation and profiling different cell types and subtypes, we uncovered a group of

461 injury-induced, WM-originated, GM-relocated astrocytes (astrocytes-GMii). These cells
462 expressed both the reactive astrocyte marker *Gfap* and the IGF signaling factor *Igfbp2*, and they
463 were molecularly distinct from the original astrocytes in the WM or the GM of the intact spinal cord
464 (Fig. 4). We explicitly showed that these GM-relocated astrocytes were migrated from the WM,
465 although not necessarily from the same segmental level of the injured spinal cord (Okada et al.,
466 2006) and unlikely through tangential astrocyte migration that was absent in adult spinal cord
467 even after injury (Tsai et al., 2012). The pseudotime trajectory and the DEG analysis strongly
468 suggested that the local environment in the GM likely triggered the transition of the migrated
469 astrocytes-WM to astrocytes-GMii, and the latter shared certain gene expression similarity with
470 the original astrocytes-GM, especially regarding the neurotrophic function in maintaining neuronal
471 synapse. However, the astrocytes-GMii were not homogeneous and the molecular features of
472 only one sub-population of these astrocytes appeared to compensate for the loss of the original
473 astrocytes-GM, while the other two sub-populations were more active in stress, immune and
474 inflammatory responses that are potentially detrimental. Thus, our findings not only provided an
475 explanation to the functional divergence of astrocytes-GMii, but also exemplified how the
476 spatiotemporal transcriptomic signatures combined with single-cell resolution may facilitate
477 subtype annotation and functional interrogation of astrocytes as well as for other cell types in SCI
478 and other diseased conditions. In addition, given that repopulation of mouse microglia was
479 recently shown to promote adult neurogenesis in traumatic brain injury (Willis et al., 2020), it is
480 tempting to propose that future efforts are warranted to induce astrocytes-GMii and manipulate
481 them to adopt a neuroprotective and pro-regenerative state that may aid spinal cord repair.

482 Taken together, this study provides the most comprehensive gene expression profiling of SCI
483 (to the best of our knowledge), involving injury time, distance, directionality, anatomic domain, cell
484 type and other dimensions. It disentangles the complex transcriptional programs induced by SCI
485 in the tissue context and establishes a spatiotemporal transcriptomic landscape for in-depth

research in the future, providing an open data resource and a platform for identifying potential targets for therapeutic intervention of SCI.

Acknowledgements

We thank Drs. J. Hu, Z. He, C. Zhang, and Misses. J Zhu and Z. Sun for assistance in mouse operation, Dr. Q. Wang for help with cryosection, Mr. G. Zhang for technical support with 10x Genomics Visium spatial RNA-seq, Dr. X. Sun for help with ISH, and Drs. Z. He, C. Liu and J. Yuan for comments and critical reading of the manuscript.

Fundings

This study was supported by grants from National Key R&D Program of China (2018YFA0801402 to G.P.); the National Natural Science Foundation of China (NSFC) (31970697 and 32270812 to Y.F., 32270854 to G.P., and 82071372 to A. L.); the Science and Technology Commission of Shanghai Municipality (201409003300, 20490712600 and 2019SHZDZX02 to Y.F.); the "Strategic Priority Research Program" of the Chinese Academy of Science (XDA16020404) to G. P.; Natural Science Foundation of Guangdong Province (2021A1515011231 to A.L. and 2019B151502054 to G.P.), the Outstanding Scholar Program of Bioland Laboratory (2018GZR110102002) and the Science and Technology Program of Guangzhou (202007030012) to A. L.

Author Contributions

AL, GP and YF conceived the research; ZW, SS, and YF designed the experiments; ZW, SS and TL performed the experiments and analyzed the data; AL, WY and YL contributed important reagents; ZL and GP performed the bioinformatic analyses; ZW, ZL, TL, GC, KZ, GP, AL and YF interpreted the results; ZW, ZL, TL, GP and YF prepared the Figures; ZW, ZL, TL, AL, GP and YF wrote the paper. All authors read and approved the final manuscript.

Competing Interests

The authors declare no competing interests.

Data and Materials Availability

All data are available in the main text or the supplementary materials. All unique and stable reagents generated in this study are available from the corresponding authors with a completed Material Transfer Agreement (MTA).

Supplemental Information

Supplemental information includes Methods and Materials, Extended Data Fig. 1-10 and Supplemental Tables 1-6.

518 **REFERENCES** *(≤50 references)*

519 Ahuja, C.S., Wilson, J.R., Nori, S., Kotter, M.R.N., Druschel, C., Curt, A., and Fehlings, M.G.
520 (2017). Traumatic spinal cord injury. Nat Rev Dis Primers. *3*, 17018.
521 Aibar, S., González-Blas, C.B., Moerman, T., Huynh-Thu, V.A., Imrichova, H., Hulselmans, G.,
522 Rambow, F., Marine, J.-C., Geurts, P., Aerts, J., et al. (2017). SCENIC: single-cell regulatory
523 network inference and clustering. Nat Methods. *14*, 1083-1086.
524 Anjum, A., Yazid, M.D., Fauzi Daud, M., Idris, J., Ng, A.M.H., Selvi Naicker, A., Ismail, O.H.R.,
525 Athi Kumar, R.K., and Lokanathan, Y. (2020). Spinal Cord Injury: Pathophysiology,
526 Multimolecular Interactions, and Underlying Recovery Mechanisms. Int J Mol Sci. *21*, 7533.
527 Asp, M., Giacomello, S., Larsson, L., Wu, C., Fürth, D., Qian, X., Wärdell, E., Custodio, J.,
528 Reimegård, J., Salmén, F., et al. (2019). A Spatiotemporal Organ-Wide Gene Expression
529 and Cell Atlas of the Developing Human Heart. Cell *179*, 1647-1660.e19.
530 Bensellam, M., Montgomery, M.K., Luzuriaga, J., Chan, J.Y., and Laybutt, D.R. (2015). Inhibitor
531 of differentiation proteins protect against oxidative stress by regulating the antioxidant-
532 mitochondrial response in mouse beta cells. Diabetologia *58*, 758-770.
533 Cable, D.M., Murray, E., Shanmugam, V., Zhang, S., Zou, L.S., Diao, M., Chen, H., Macosko,
534 E.Z., Irizarry, R.A., and Chen, F. (2022a). Cell type-specific inference of differential
535 expression in spatial transcriptomics. Nat Methods. *19*, 1076-1087.
536 Cable, D.M., Murray, E., Zou, L.S., Goeva, A., Macosko, E.Z., Chen, F., and Irizarry, R.A. (2022b).
537 Robust decomposition of cell type mixtures in spatial transcriptomics. Nat Biotechnol. *40*,
538 517-526.
539 Chen, W.-T., Lu, A., Craessaerts, K., Pavie, B., Sala Frigerio, C., Corthout, N., Qian, X., Laláková,
540 J., Kühnemund, M., Voytyuk, I., et al. (2020). Spatial Transcriptomics and In Situ Sequencing
541 to Study Alzheimer's Disease. Cell *182*, 976-991.e19.

542 Denisenko, E., Guo, B.B., Jones, M., Hou, R., de Kock, L., Lassmann, T., Poppe, D., Clément,
543 O., Simmons, R.K., Lister, R., et al. (2020). Systematic assessment of tissue dissociation
544 and storage biases in single-cell and single-nucleus RNA-seq workflows. Genome Biol. *21*,
545 130.
546 Escartin, C., Galea, E., Lakatos, A., O'Callaghan, J.P., Petzold, G.C., Serrano-Pozo, A.,
547 Steinhäuser, C., Volterra, A., Carmignoto, G., Agarwal, A., et al. (2021). Reactive astrocyte
548 nomenclature, definitions, and future directions. Nature Neurosci. *24*, 312-325.
549 Fawkner-Corbett, D., Antanaviciute, A., Parikh, K., Jagielowicz, M., Gerós, A.S., Gupta, T.,
550 Ashley, N., Khamis, D., Fowler, D., Morrissey, E., et al. (2021). Spatiotemporal analysis of
551 human intestinal development at single-cell resolution. Cell *184*, 810-826.e23.
552 Frattini, V., Pagnotta, S.M., Tala, Fan, J.J., Russo, M.V., Lee, S.B., Garofano, L., Zhang, J., Shi,
553 P., Lewis, G., et al. (2018). A metabolic function of FGFR3-TACC3 gene fusions in cancer.
554 Nature *553*, 222-227.
555 Gong, L., Gu, Y., Han, X., Luan, C., Liu, C., Wang, X., Sun, Y., Zheng, M., Fang, M., Yang, S.,
556 et al. (2022). Spatiotemporal Dynamics of the Molecular Expression Pattern and Intercellular
557 Interactions in the Glial Scar Response to Spinal Cord Injury. Neurosci Bull. 1-32.
558 Hasel, P., Rose, I.V.L., Sadick, J.S., Kim, R.D., and Liddelow, S.A. (2021). Neuroinflammatory
559 astrocyte subtypes in the mouse brain. Nat Neurosci. *24*, 1475-1487.
560 Jin, S., Guerrero-Juarez, C.F., Zhang, L., Chang, I., Ramos, R., Kuan, C.-H., Myung, P., Plikus,
561 M.V., and Nie, Q. (2021). Inference and analysis of cell-cell communication using CellChat.
562 Nat Commun. *12*, 1088.
563 Kaufmann, M., Schaupp, A.-L., Sun, R., Coscia, F., Dendrou, C.A., Cortes, A., Kaur, G., Evans,
564 H.G., Mollbrink, A., Navarro, J.F., et al. (2022). Identification of early neurodegenerative
565 pathways in progressive multiple sclerosis. Nat Neurosci. *25*, 944-955.
566 Lacroix, S., Hamilton, L.K., Vaugeois, A., Beaudoin, S., Breault-Dugas, C., Pineau, I., Lévesque,
567 S.A., Grégoire, C.-A., and Fernandes, K.J.L. (2014). Central Canal Ependymal Cells

568 Proliferate Extensively in Response to Traumatic Spinal Cord Injury but Not Demyelinating
569 Lesions. PLoS One *9*, e85916.
570 Langfelder, P., and Horvath, S. (2008). WGCNA: an R package for weighted correlation network
571 analysis. BMC Bioinformatics *9*, 559.
572 Li, C., Wu, Z., Zhou, L., Shao, J., Hu, X., Xu, W., Ren, Y., Zhu, X., Ge, W., Zhang, K., et al.
573 (2022a). Temporal and spatial cellular and molecular pathological alterations with single-cell
574 resolution in the adult spinal cord after injury. Signal Transduct Target Ther. *7*, 65.
575 Li, L., Zhou, J., Han, L., Wu, X., Shi, Y., Cui, W., Zhang, S., Hu, Q., Wang, J., Bai, H., et al.
576 (2022b). The Specific Role of Reactive Astrocytes in Stroke. Front Cell Neurosci. *16*, 850866.
577 Li, Z., and Peng, G. (2021). Spatial transcriptomics: new dimension of understanding biological
578 complexity. Biophysics Reports *7*, 1-17.
579 Liu, T., Zhang, L., Joo, D., and Sun, S.-C. (2017). NF-κB signaling in inflammation. Sig Transduct
580 Target Ther *2*, 17023.
581 Macdonald, C.D., Falconer, A.M.D., Chan, C.M., Wilkinson, D.J., Skelton, A., Reynard, L.,
582 Litherland, G.J., Europe-Finner, G.N., and Rowan, A.D. (2018). Cytokine-induced cysteine-
583 serine-rich nuclear protein-1 (CSRNP1) selectively contributes to MMP1 expression in
584 human chondrocytes. PLoS One *13*, e0207240.
585 Maniatis, S., Äijö, T., Vickovic, S., Braine, C., Kang, K., Mollbrink, A., Fagegaltier, D.,
586 Andrusivová, Ž., Saarenpää, S., Saiz-Castro, G., et al. (2019). Spatiotemporal dynamics of
587 molecular pathology in amyotrophic lateral sclerosis. Science *364*, 89-93.
588 Matson, K.J.E., Russ, D.E., Kathe, C., Hua, I., Maric, D., Ding, Y., Krynitsky, J., Pursley, R.,
589 Sathyamurthy, A., Squair, J.W., et al. (2022). Single cell atlas of spinal cord injury in mice
590 reveals a pro-regenerative signature in spinocerebellar neurons. Nat Commun. *13*, 5628.
591 Meletis, K., Barnabé-Heider, F., Carlén, M., Evergren, E., Tomilin, N., Shupliakov, O., and Frisén,
592 J. (2008). Spinal Cord Injury Reveals Multilineage Differentiation of Ependymal Cells. PLoS
593 Biol. *6*, e182.

594 Milich, L.M., Choi, J.S., Ryan, C., Cerqueira, S.R., Benavides, S., Yahn, S.L., Tsoulfas, P., and
595 Lee, J.K. (2021). Single-cell analysis of the cellular heterogeneity and interactions in the
596 injured mouse spinal cord. J Exp Med. *218*, e20210040.
597 Molofsky, A.V., Krenick, R., Ullian, E., Tsai, H., Deneen, B., Richardson, W.D., Barres, B.A., and
598 Rowitch, D.H. (2012). Astrocytes and disease: a neurodevelopmental perspective. Genes
599 Dev. *26*, 891-907.
600 Molofsky, A.V., Glasgow, S.M., Chaboub, L.S., Tsai, H., Murnen, A.T., Kelley, K.W., Fancy,
601 S.P.J., Yuen, T.J., Madireddy, L., Baranzini, S., et al. (2013). Expression profiling of Aldh1l1-
602 precursors in the developing spinal cord reveals glial lineage-specific genes and direct Sox9-
603 Nfe2l1 interactions. Glia *61*, 1518-1532.
604 Monje, M. (2018). Myelin Plasticity and Nervous System Function. Annu Rev Neurosci.*41*, 61-
605 76.
606 Moor, A.E., and Itzkovitz, S. (2017). Spatial transcriptomics: paving the way for tissue-level
607 systems biology. Curr Opin Biotechnol. *46*, 126-133.
608 Noristani, H.N., Sabourin, J.C., Boukhaddaoui, H., Chan-Seng, E., Gerber, Y.N., and Perrin, F.E.
609 (2016). Spinal cord injury induces astroglial conversion towards neuronal lineage. Mol
610 Neurodegener. *11*, 68.
611 Okada, S., Nakamura, M., Katoh, H., Miyao, T., Shimazaki, T., Ishii, K., Yamane, J., Yoshimura,
612 A., Iwamoto, Y., Toyama, Y., et al. (2006). Conditional ablation of Stat3 or Socs3 discloses
613 a dual role for reactive astrocytes after spinal cord injury. Nat Medi. *12*, 829-834.
614 Ortiz, C., Navarro, J.F., Jurek, A., Märtin, A., Lundeberg, J., and Meletis, K. (2020). Molecular
615 atlas of the adult mouse brain. Sci Adv. *6*, eabb3446.
616 Peng, G., Suo, S., Cui, G., Yu, F., Wang, R., Chen, J., Chen, S., Liu, Z., Chen, G., Qian, Y., et
617 al. (2019). Molecular architecture of lineage allocation and tissue organization in early mouse
618 embryo. Nature *572*, 528-532.

619 Pierrot, N. (2011). Amyloid precursor protein regulates SREBP-mediated neuronal lipid
620 homeostasis in mice and humans. Alzheimers Dement. *7*, S572.
621 Rao, A., Barkley, D., França, G.S., and Yanai, I. (2021). Exploring tissue architecture using
622 spatial transcriptomics. Nature *596*, 211-220.
623 Ratz, M., von Berlin, L., Larsson, L., Martin, M., Westholm, J.O., La Manno, G., Lundeberg, J.,
624 and Frisén, J. (2022). Clonal relations in the mouse brain revealed by single-cell and spatial
625 transcriptomics. Nat Neurosci. *25*, 285-294.
626 Rosenberg, A.B., Roco, C.M., Muscat, R.A., Kuchina, A., Sample, P., Yao, Z., Graybuck, L.T.,
627 Peeler, D.J., Mukherjee, S., Chen, W., et al. (2018). Single-cell profiling of the developing
628 mouse brain and spinal cord with split-pool barcoding. Science *360*, 176-182.
629 Sathyamurthy, A., Johnson, K.R., Matson, K.J.E., Dobrott, C.I., Li, L., Ryba, A.R., Bergman, T.B.,
630 Kelly, M.C., Kelley, M.W., and Levine, A.J. (2018). Massively Parallel Single Nucleus
631 Transcriptional Profiling Defines Spinal Cord Neurons and Their Activity during Behavior. Cell
632 Reports *22*, 2216-2225.
633 Saul, M.C., Seward, C.H., Troy, J.M., Zhang, H., Sloofman, L.G., Lu, X., Weisner, P.A., Caetano-
634 Anolles, D., Sun, H., Zhao, S.D., et al. (2017). Transcriptional regulatory dynamics drive
635 coordinated metabolic and neural response to social challenge in mice. Genome Res. *27*,
636 959-972.
637 Shaulian, E., and Karin, M. (2001). AP-1 in cell proliferation and survival. Oncogene *20*, 2390-
638 2400.
639 Sidoryk-wegrzynowicz, M., Wegrzynowicz, M., Lee, E., Bowman, A.B., and Aschner, M. (2011).
640 Role of Astrocytes in Brain Function and Disease. Toxicol Pathol. *39*, 115-123.
641 Soderblom, C., Luo, X., Blumenthal, E., Bray, E., Lyapichev, K., Ramos, J., Krishnan, V., Lai-
642 Hsu, C., Park, K.K., Tsoulfas, P., et al. (2013). Perivascular Fibroblasts Form the Fibrotic
643 Scar after Contusive Spinal Cord Injury. J Neurosci. *33*, 13882-13887.

644 Stogsdill, J.A., Ramirez, J., Liu, D., Kim, Y.H., Baldwin, K.T., Enustun, E., Ejikeme, T., Ji, R.-R.,
645 and Eroglu, C. (2017). Astrocytic neuroligins control astrocyte morphogenesis and
646 synaptogenesis. Nature *551*, 192-197.
647 Street, K., Risso, D., Fletcher, R.B., Das, D., Ngai, J., Yosef, N., Purdom, E., and Dudoit, S.
648 (2018). Slingshot: cell lineage and pseudotime inference for single-cell transcriptomics. BMC
649 Genomics *19*, 477.
650 Sykes, S.M., Di Marcantonio, D., Martinez, E., Huhn, J., Gupta, A., and Mistry, R. (2018). JUN
651 and ATF3 Regulate the Transcriptional Output of the Unfolded Protein Response to Support
652 Acute Myeloid Leukemia. Blood *132*, 1327.
653 Tavares-Ferreira, D., Shiers, S., Ray, P.R., Wangzhou, A., Jeevakumar, V., Sankaranarayanan,
654 I., Cervantes, A.M., Reese, J.C., Chamessian, A., Copits, B.A., et al. (2022). Spatial
655 transcriptomics of dorsal root ganglia identifies molecular signatures of human nociceptors.
656 Sci Transl Med. *14*, eabj8186.
657 Tsai, H.-H. ., Li, H., Fuentealba, L.C., Molofsky, A.V., Taveira-Marques, R., Zhuang, H., Tenney,
658 A., Murnen, A.T., Fancy, S.P.J., Merkle, F., et al. (2012). Regional Astrocyte Allocation
659 Regulates CNS Synaptogenesis and Repair. Science *337*, 358-362.
660 Wang, J.-J., Ye, G., Ren, H., An, C.-R., Huang, L., Chen, H., Zhang, H., Lin, J.-X., Shen, X.,
661 Heng, B.C., et al. (2021). Molecular Expression Profile of Changes in Rat Acute Spinal Cord
662 Injury. Front Cell Neurosci. *15*, 720271.
663 Willemsen, L., and Winther, M.P. (2020). Macrophage subsets in atherosclerosis as defined by
664 single-cell technologies. J Pathol. *250*, 705-714.
665 Williams, C.G., Lee, H.J., Asatsuma, T., Vento-Tormo, R., and Haque, A. (2022). An introduction
666 to spatial transcriptomics for biomedical research. Genome Med. *14*, 68.
667 Willis, E.F., MacDonald, K.P.A., Nguyen, Q.H., Garrido, A.L., Gillespie, E.R., Harley, S.B.R.,
668 Bartlett, P.F., Schroder, W.A., Yates, A.G., Anthony, D.C., et al. (2020). Repopulating
669 Microglia Promote Brain Repair in an IL-6-Dependent Manner. Cell *180*, 833-846.e16.

670 Yan, D., Wang, H.-W., Bowman, Robert L., and Joyce, Johanna A. (2016). STAT3 and STAT6
671 Signaling Pathways Synergize to Promote Cathepsin Secretion from Macrophages via IRE1α
672 Activation. Cell Rep. *16*, 2914-2927.
673 Yáñez, A., and Goodridge, H.S. (2016). Interferon regulatory factor 8 and the regulation of
674 neutrophil, monocyte, and dendritic cell production. Curr Opin Hematol. *23*, 11-17.
675 Yoon, H., Walters, G., Paulsen, A.R., and Scarisbrick, I.A. (2017). Astrocyte heterogeneity
676 across the brain and spinal cord occurs developmentally, in adulthood and in response to
677 demyelination. PLoS One *12*, e0180697.
678 Zeisel, A., Hochgerner, H., Lönnerberg, P., Johnsson, A., Memic, F., van der Zwan, J., Häring,
679 M., Braun, E., Borm, L.E., La Manno, G., et al. (2018). Molecular Architecture of the Mouse
680 Nervous System. Cell *174*, 999-1014.e22.
681 Zhang, K., Jiang, M., and Fang, Y. (2021). The Drama of Wallerian Degeneration: The Cast,
682 Crew, and Script. Annu Rev Genet. *55*, 93-113.
683 Zhou, Q., Wang, S., and Anderson, D.J. (2000). Identification of a Novel Family of
684 Oligodendrocyte Lineage-Specific Basic Helix-Loop-Helix Transcription Factors. Neuron *25*,
685 331-343.

686 **FIGURE LEGENDS (< 250 words each)**

687 **Fig. 1. Spatiotemporal transcriptomics and molecular clusters of mouse SCI using Visium**
688 (**a**) A carton of the mouse SCI model and the spinal cord sections obtained in this spatial
689 transcriptomic study. (**b**) A schematic of the Visium Gene Expression slide and the acquisition of
690 the mouse SCI sections for RNA-sequencing. (**c**) The main workflow of the spatial transcriptomic
691 data analyses. (**d**) The UMAP plot of the 22,820 transcriptomic profiles (one profile for each spatial
692 spot) of all the SCI samples identified 7 spatiotemporal clusters. (**e**) The clusters are color coded
693 and shown in the spatial view of the spinal cord sections at the indicated locations and time points
694 after injury. (**f**) A cartoon showing the main anatomic regions of the spinal cord: WM, white matter;
695 MG, middle grey; DH, dorsal horn; VH, ventral horn. (**g-j**) The UMAP plots of the spatial spots
696 were colored according to anatomic region (**g**), time after injury (**h**), directionality (**i**) and distance
697 to the injury site (**j**). (**k**) Quantification of the numbers of the spatial spots in each cluster at the
698 indicated time points. (**l**) The heatmap showing the expression levels of the top 10 CEGs (left)
699 and the dot-plot showing the top 5 GO terms (right) for each of the 7 spatiotemporal clusters. (**m**)
700 The spatial view of the gene expression levels in the spatiotemporal transcriptomics (ST, left) and
701 *in situ* hybridization (ISH, right) of four representative anatomic markers as indicated. Scale bar:
702 500 μm. SCI, spinal cord injury; hpi: hours post injury; UMI, unique molecular identifier; UMAP,
703 uniform manifold approximation and projection; CEGs, cluster-enriched genes; GO terms, gene
704 ontology terms; *p*. adjust, adjusted *p* value.

705

706 **Fig. 2. Spatiotemporal analyses of gene co-expression dynamics and regulatory networks**
707 **in SCI**

708 (**a**) Heatmap showing the pairwise-correlation network of the 33 SCI spatiotemporal CGMs. (**b**)
709 The Pearson correlation coefficients between each CGM and the four anatomic domains at the
710 indicated time points in SCI. (**c-e**) The molecular features of three representative CGMs: CGM13

711 (**c**), CGM9 (**d**) and CGM11 (**e**). From left to right: Left, the spatial view of average levels of the
712 genes expressed in the indicated CGM during the process of SCI; middle, the ridge plot
713 quantitatively illustrating the density distribution of the CGM expression within the 4 anatomic
714 domains at the indicated time points of SCI; right, the representative GO terms (top) and the gene
715 network showing the highest 50 connectivity weights (bottom) of the indicated CGM. The number
716 of genes in each CGM is shown in the parentheses. (**f**) The CSI heatmap of 147 transcription
717 regulons grouped into 7 RMs by hierarchical clustering. (**g**) The heatmap of the overall activity of
718 each RM enriched in the four anatomic domains at the indicated time points of SCI. (**h**) The spatial
719 view of the average regulon activity of RM2 at the indicated time points of SCI. The number of
720 regulons in RM2 is shown in the parentheses. (**i**) The Pearson correlation networks and the CSI
721 connectivity degree of the transcription regulons within and across the 7 RMs. CGM, co-
722 expressed gene module; CSI, connectivity specificity index; RM, regulon module.
723

724 **Fig. 3. SCI-induced multicellular transcriptional responses and cell-cell communications**
725 (**a**) The spatial view of the proportions of cell types (indicated as pie chart) in each spot of the
726 uninjured spinal cord (0 hpi, -0.5 mm). (**b**) The spatial distributions of the representative spinal
727 cord cell types from (a); for more, see Extended Data Fig. 7-8. (**c**) The fractions (%) of different
728 cell types at indicated time points in SCI. (**d**) A schematic cartoon illustrating the main procedure
729 for the spatial-aware cell-cell communication (SA-CCC) analysis that evaluates *in situ* intercellular
730 communication by testing the statistical significance of the co-occurrence of a cell-type pair and
731 a L_R pair. (**e**) The SA-CCC networks at each indicated time point in SCI. The size of the orange
732 circles represents the number of potential L_R pairs expressed in each cell-type pair. For the
733 connecting lines, the thickness denotes the GeoM of the significance of the interaction and the
734 shade indicates the average expression levels of the L_R pairs for each cell-type pair. (**f**) Dot
735 plots showing the top 2 (*p*. value) interacting L_R pairs in each cell-type pair at the indicated time
736 points in SCI. Color indicates the average expression levels of each L_R pair that are expressed

737 in the indicated, colocalized cell-type pairs. (**g**) The three major classes of SCI-induced changes
738 in the expression of the L_R pairs, summarized from (f). (**h**) Left: the spatial views of the
739 interaction of a representative Class-I L_R pair *Spp1_Cd44* in (g); right: the spatial distributions
740 of the major cell-type pairs hosting the L_R pair of *Spp1_Cd44* along the time during SCI. Astro,
741 astrocytes; WM, white matter; GM, grey matter; H-Microglia, homeostatic microglia; R-Microglia,
742 reactive microglia; SA-CCC, spatial-aware cell-cell communication; GeoM, geometric mean; EM,
743 assembly mean; L_R pair, ligand_receptor pair.
744

745 **Fig. 4. Identification and molecular profiling of the SCI-induced astrocytes-GMii with**
746 **spatial transcriptomics and scRNA-seq integration**

747 (**a-d**) The spatiotemporal distributions astrocytes-WM (**a**) and astrocytes-GM (**c**), validated with
748 ISH of *Gfap* for astrocytes-WM (**b**) and *Pla2g7* for astrocytes-GM (**d**). Scale bars: 500 μm. (**e**) An
749 overview of the comprehensive spatial and single-cell analyses (in Fig. 4f-q and Extended Data
750 Fig. 9) for the identification and characterization of the SCI-induced astrocytes-GMii. (**f**) From left
751 to right: left, the geometric proportions of the cell-type pairs of “astrocyte-GM_neuron” and
752 “astrocyte-WM_neuron”; middle, the expression levels of the individual ligand, receptor, and their
753 geometric mean of the L_R pair of *Nrxn3_Nlgn3*; right, the average expression of the
754 *Nrxn3_Nlgn3* pair within the indicated co-localized cell-type pairs along the time in SCI. (**g, h**) The
755 spatiotemporal dynamics of the proliferation (**g**) and migration (**h**) scores in SCI. (**i**) The 317
756 astrocyte deconvolution marker genes are clustered into 4 SA groups based on their bulk
757 expression levels in the spatial spots that contain molecularly-defined astrocytes-WM, and their
758 correlations with the injury time and the anatomic domains of WM and GM are shown. (**j, k**) The
759 UMAP re-clustering (**j**) and pseudotime trajectory (**k**) analyses of the astrocytes-*Gfap* in the SCI
760 single-cell dataset (Milich et al., 2021) identify distinct populations of astrocytes-WM and
761 astrocytes-GMii sharing a continuous cell lineage. (**l**) The top 50 most dramatically-altered genes
762 along the trajectory in (k). Of them, an example of *Igfbp2* is examined by FISH in (m). (**m**)

763 Representative confocal images of immunostaining of GFAP combined with FISH of *Igfbp2* of the
764 mouse spinal cord (-1.0 mm section) at the indicated time points in SCI. The white-boxed areas
765 are shown in a higher magnification in the zoom-ins and the 3D rendering of a "GFAP$^+$-*Igfbp2*$^+$"
766 cell at 72 hpi (yellow box) is shown, with DAPI staining to indicate the location of the nucleus. The
767 average numbers of the indicated genotypes of cells per mm^2 of the mouse spinal cord area and
768 the percentage of "GFAP$^+$-*Igfbp2*$^+$" cells to total cell counts (indicated by DAPI) at the indicated
769 time points in SCI are quantified. Mean ± SEM; n = 6; *$p < 0.05$ and ***$p < 0.001$; one-way ANOVA.
770 Scale bars: 10 μm in 3D rendering, 25 μm in zoom-ins, and 200 μm in the rest. (**n**) GO term
771 analysis of the unique and shared DEGs (left) and the heatmap showing the average normalized
772 expression levels of the DEGs (right) associated with the three spatiotemporally-defined groups
773 of astrocytes-WM, -GM and -GMii. The DEGs that are cross-referenced as pro-inflammatory (red),
774 trophic (red) or protective (in bold) genes (Kaufmann et al., 2022) are highlighted. (**o**) The UMAP
775 re-projection of the astrocytes-*Gfap* in the scRNA-seq dataset (Milich et al., 2021) reveals 5
776 casual sub-clusters. (**p**) The violin plots showing the distributions of the GMii score of the 5
777 astrocyte sub-clusters in (o). (**q**) Heatmap showing the average expression levels of the top 10
778 (*p*. adjust < 0.05) DEGs (left) and GO terms (right) for each sub-cluster identified in (o). Astro,
779 astrocytes; WM, white matter; GM, grey matter; Astro-GMii, injury-induced GM-relocated
780 astrocytes. ISH, *in situ* hybridization; SA, spatiotemporally-separate astrocyte; FISH,
781 fluorescence ISH; DEGs, differentially expressed genes.

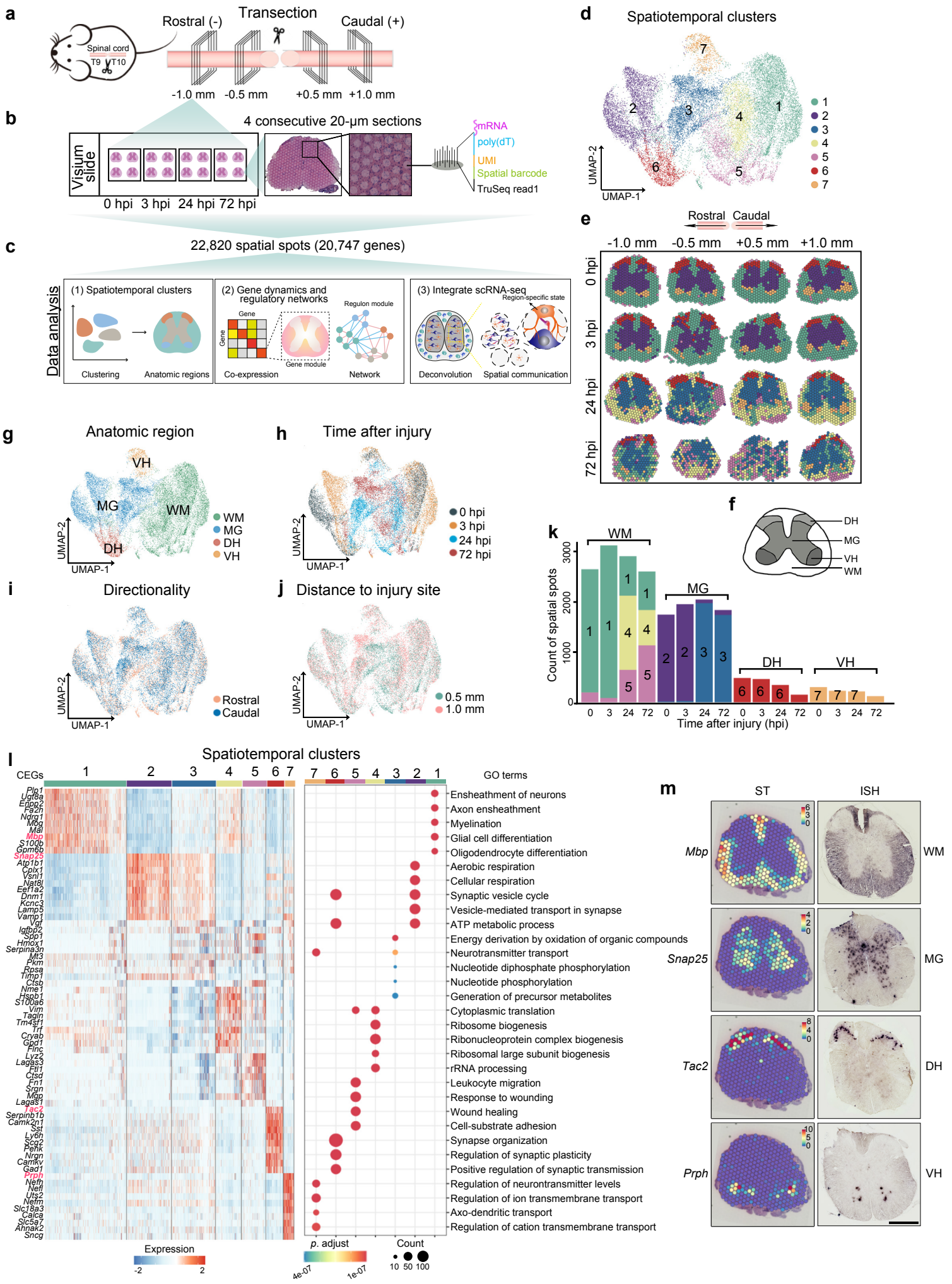
a
Rostral (-)
Transection
Caudal (+)
Spinal cord
T9
T10
-1.0 mm
-0.5 mm
+0.5 mm
+1.0 mm
b
4 consecutive 20-µm sections
Visium slide
0 hpi
3 hpi
24 hpi
72 hpi
mRNA
poly(dT)
UMI
Spatial barcode
TruSeq read1
c
22,820 spatial spots (20,747 genes)
Data analysis
(1) Spatiotemporal clusters
Clustering
Anatomic regions
(2) Gene dynamics and regulatory networks
Gene
Gene module
Regulon module
Co-expression
Network
(3) Integrate scRNA-seq
Region-specific state
Deconvolution
Spatial communication
d
Spatiotemporal clusters
UMAP-2
UMAP-1
e
Rostral
Caudal
-1.0 mm
-0.5 mm
+0.5 mm
+1.0 mm
0 hpi
3 hpi
24 hpi
72 hpi
f
DH
MG
VH
WM
g
Anatomic region
VH
MG
WM
DH
h
Time after injury
0 hpi
3 hpi
24 hpi
72 hpi
i
Directionality
Rostral
Caudal
j
Distance to injury site
0.5 mm
1.0 mm
k
Count of spatial spots
Time after injury (hpi)
l
Spatiotemporal clusters
CEGs
GO terms
Ensheathment of neurons
Axon ensheathment
Myelination
Glial cell differentiation
Oligodendrocyte differentiation
Aerobic respiration
Cellular respiration
Synaptic vesicle cycle
Vesicle-mediated transport in synapse
ATP metabolic process
Energy derivation by oxidation of organic compounds
Neurotransmitter transport
Nucleotide diphosphate phosphorylation
Nucleotide phosphorylation
Generation of precursor metabolites
Cytoplasmic translation
Ribosome biogenesis
Ribonucleoprotein complex biogenesis
Ribosomal large subunit biogenesis
rRNA processing
Leukocyte migration
Response to wounding
Wound healing
Cell-substrate adhesion
Synapse organization
Regulation of synaptic plasticity
Positive regulation of synaptic transmission
Regulation of neurotransmitter levels
Regulation of ion transmembrane transport
Axo-dendritic transport
Regulation of cation transmembrane transport
Expression
p. adjust
Count
m
ST
ISH
Mbp
Snap25
Tac2
Prph
WM
MG
DH
VH

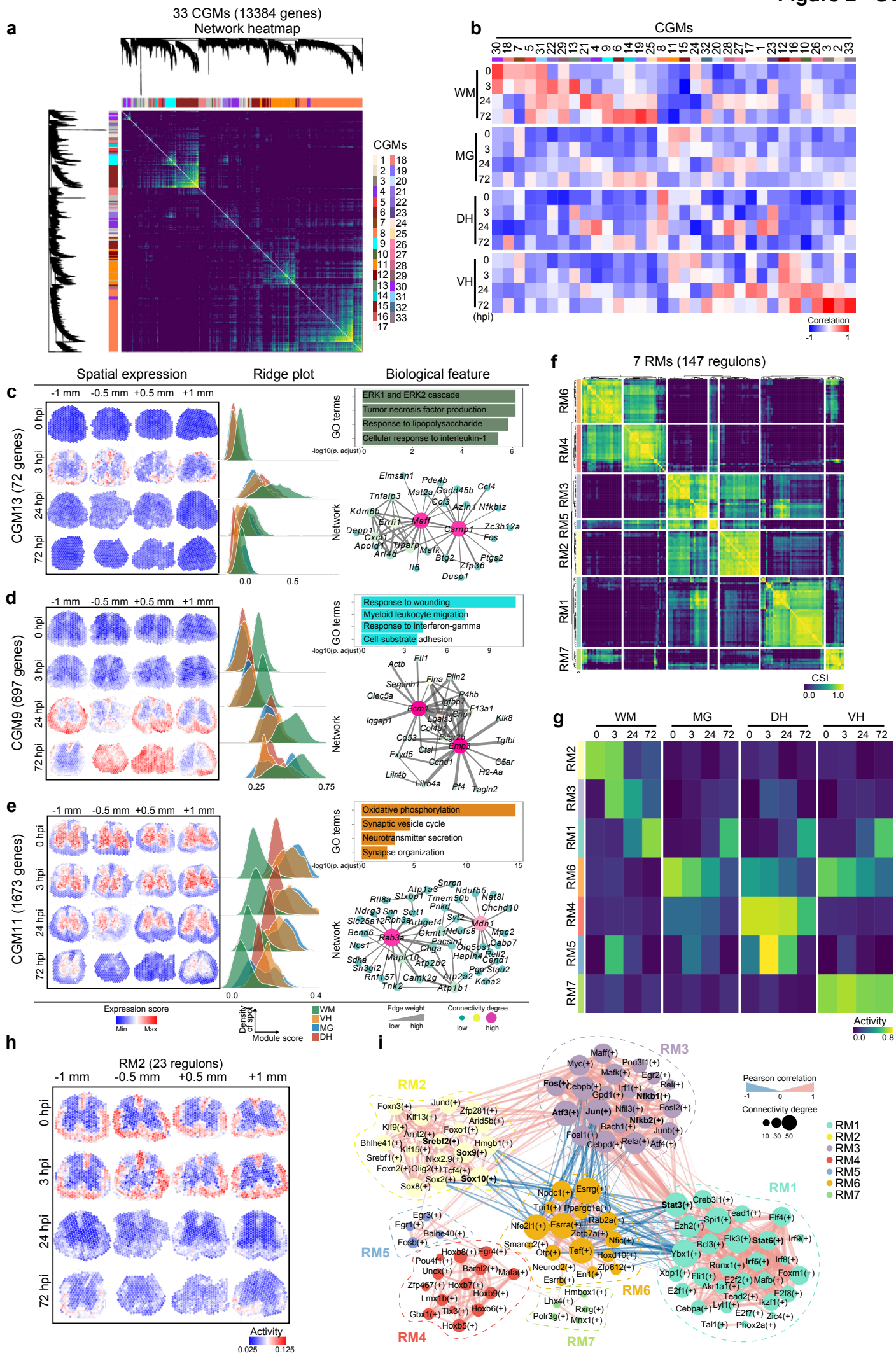
a
33 CGMs (13384 genes)
Network heatmap
CGMs
b
CGMs
WM
MG
DH
VH
(hpi)
Correlation
c
Spatial expression
Ridge plot
Biological feature
CGM13 (72 genes)
-1 mm
-0.5 mm
+0.5 mm
+1 mm
0 hpi
3 hpi
24 hpi
72 hpi
GO terms
ERK1 and ERK2 cascade
Tumor necrosis factor production
Response to lipopolysaccharide
Cellular response to interleukin-1
Network
d
CGM9 (697 genes)
Response to wounding
Myeloid leukocyte migration
Response to interferon-gamma
Cell-substrate adhesion
e
CGM11 (1673 genes)
Oxidative phosphorylation
Synaptic vesicle cycle
Neurotransmitter secretion
Synapse organization
Expression score
Min
Max
Density of spot
Module score
WM
VH
MG
DH
Edge weight
low
high
Connectivity degree
f
7 RMs (147 regulons)
RM6
RM4
RM3
RM5
RM2
RM1
RM7
CSI
g
WM
MG
DH
VH
Activity
h
RM2 (23 regulons)
Activity
i
RM3
RM2
RM1
RM5
RM6
RM4
RM7
Pearson correlation
Connectivity degree
RM1
RM2
RM3
RM4
RM5
RM6
RM7

Figure 3 - SCI ST

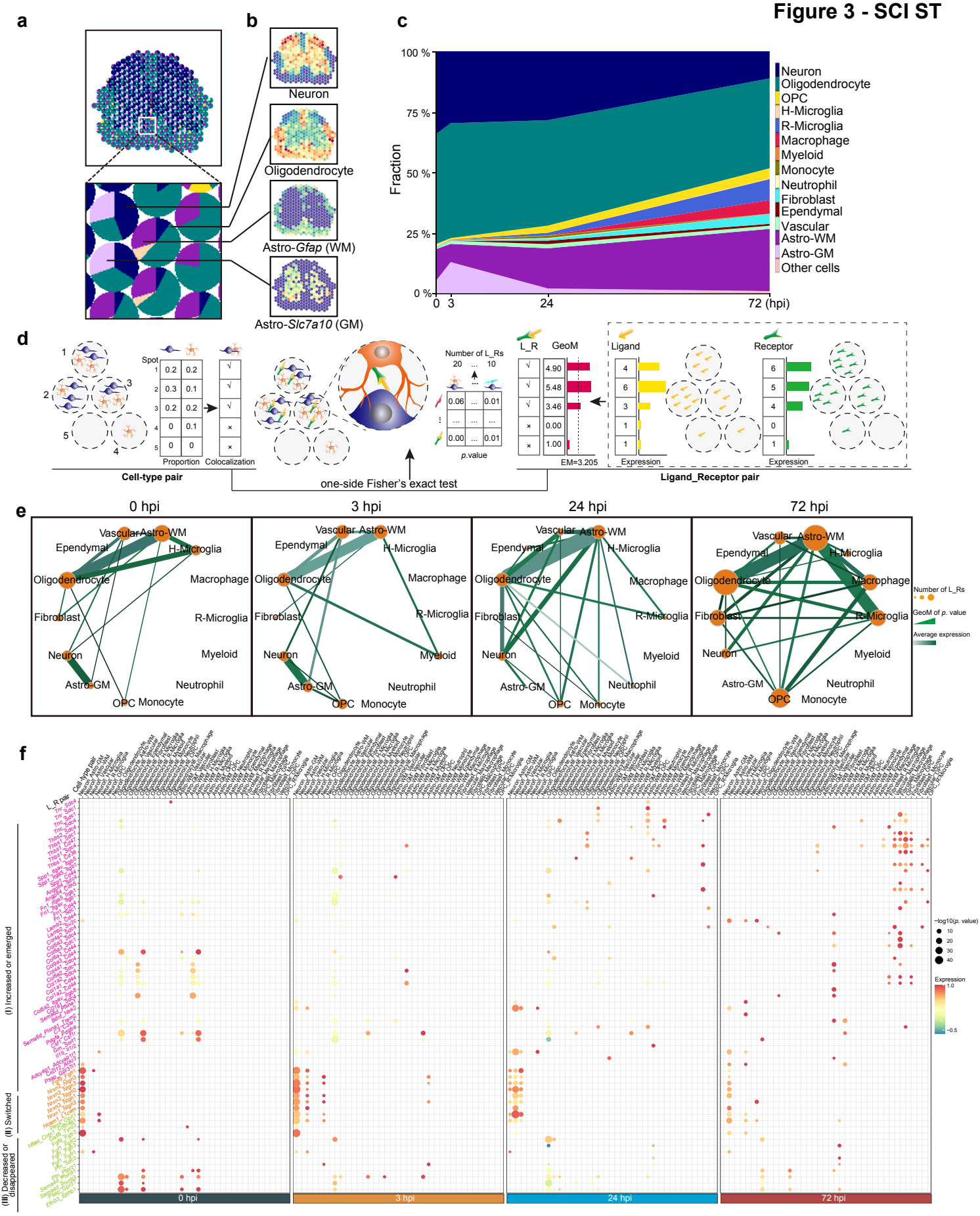

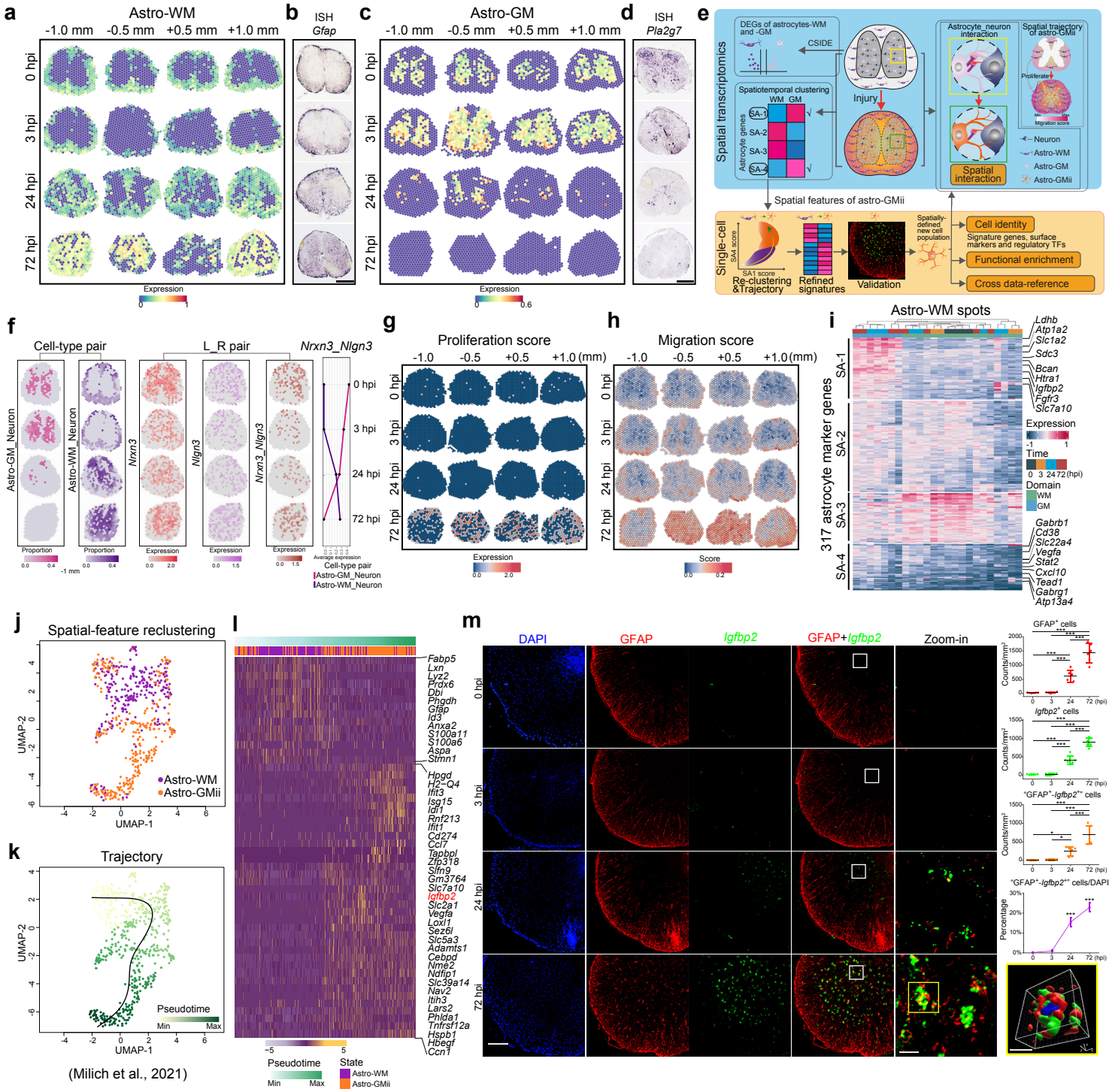
a
Astro-WM
-1.0 mm -0.5 mm +0.5 mm +1.0 mm
0 hpi
3 hpi
24 hpi
72 hpi
Expression
b
ISH
Gfap
c
Astro-GM
-1.0 mm -0.5 mm +0.5 mm +1.0 mm
0 hpi
3 hpi
24 hpi
72 hpi
Expression
d
ISH
Pla2g7
e
Spatial transcriptomics
DEGs of astrocytes-WM and -GM
CSIDE
Spatiotemporal clustering
WM GM
SA-1
SA-2
SA-3
SA-4
Astrocyte genes
Injury
Astrocyte_neuron interaction
Spatial trajectory of astro-GMii
Proliferate
Migration score
Spatial interaction
Neuron
Astro-WM
Astro-GM
Astro-GMii
Spatial features of astro-GMii
Single-cell
SA4 score
SA1 score
Re-clustering &Trajectory
Refined signatures
Validation
Spatially-defined new cell population
Cell identity
Signature genes, surface markers and regulatory TFs
Functional enrichment
Cross data-reference
f
Cell-type pair
L_R pair
Nrxn3_Nlgn3
Astro-GM_Neuron
Astro-WM_Neuron
Nrxn3
Nlgn3
Nrxn3_Nlgn3
Proportion
Expression
0 hpi
3 hpi
24 hpi
72 hpi
Cell-type pair
Astro-GM_Neuron
Astro-WM_Neuron
g
Proliferation score
-1.0 -0.5 +0.5 +1.0 (mm)
0 hpi
3 hpi
24 hpi
72 hpi
Expression
h
Migration score
-1.0 -0.5 +0.5 +1.0 (mm)
0 hpi
3 hpi
24 hpi
72 hpi
Score
i
Astro-WM spots
317 astrocyte marker genes
SA-1
SA-2
SA-3
SA-4
Ldhb
Atp1a2
Slc1a2
Sdc3
Bcan
Htra1
Igfbp2
Fgfr3
Slc7a10
Gabrb1
Cd38
Slc22a4
Vegfa
Stat2
Cxcl10
Tead1
Gabrg1
Atp13a4
Expression
Time
0 3 24 72 (hpi)
Domain
WM
GM
j
Spatial-feature reclustering
UMAP-1
UMAP-2
Astro-WM
Astro-GMii
k
Trajectory
UMAP-1
UMAP-2
Pseudotime
Min
Max
(Milich et al., 2021)
l
Fabp5
Lxn
Lyz2
Prdx6
Dbi
Phgdh
Gfap
Id3
Anxa2
S100a11
S100a6
Aspa
Stmn1
Hpgd
H2-Q4
Ifit3
Isg15
Idi1
Rnf213
Ifit1
Cd274
Ccl7
Tapbpl
Zfp318
Slfn9
Gm3764
Slc7a10
Igfbp2
Slc2a1
Vegfa
Loxl1
Sez6l
Slc5a3
Adamts1
Cebpd
Nme2
Ndfip1
Slc39a14
Nav2
Itih3
Lars2
Phlda1
Tnfrsf12a
Hspb1
Hbegf
Ccn1
Pseudotime
Min
Max
State
Astro-WM
Astro-GMii
m
DAPI
GFAP
Igfbp2
GFAP+Igfbp2
Zoom-in
0 hpi
3 hpi
24 hpi
72 hpi
GFAP+ cells
Igfbp2+ cells
GFAP+-Igfbp2++ cells
GFAP+-Igfbp2++ cells/DAPI
Counts/mm²
Percentage
72 (hpi)

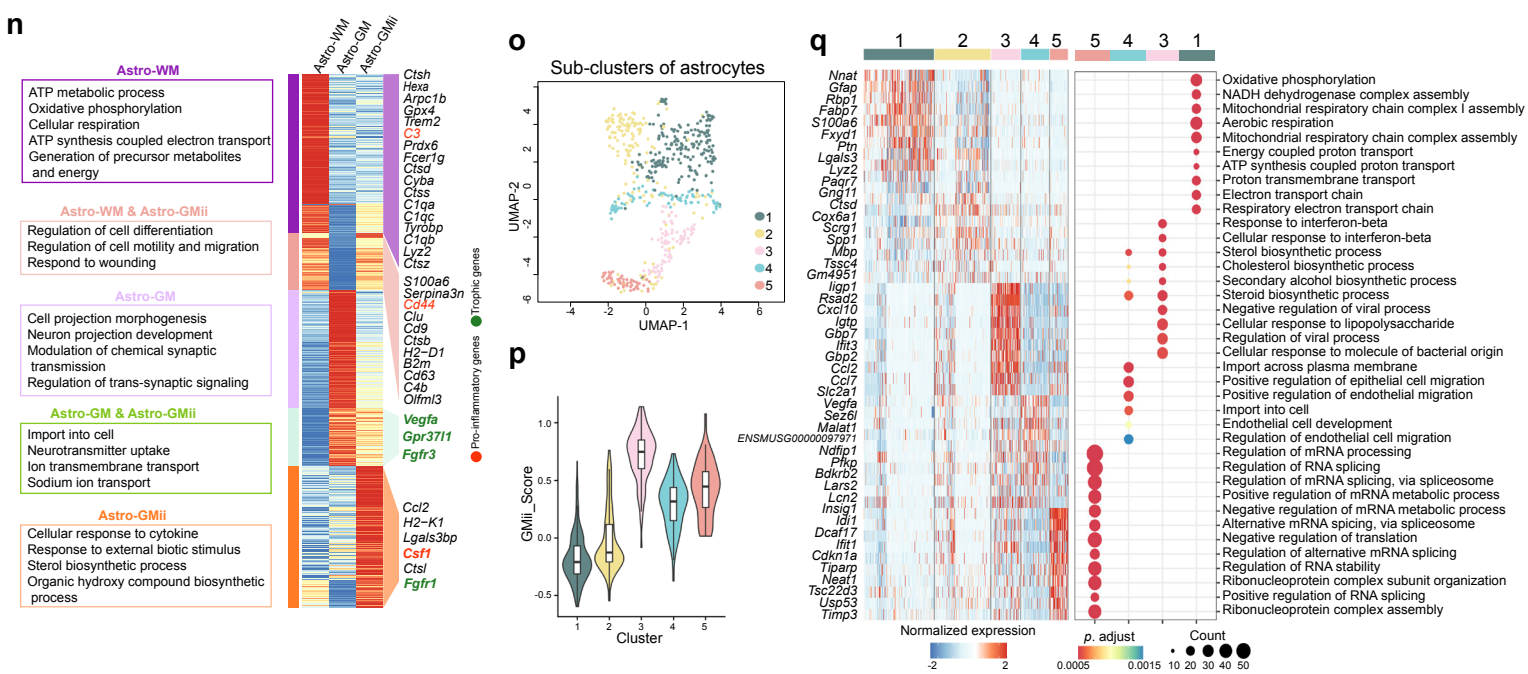
n
Astro-WM
ATP metabolic process
Oxidative phosphorylation
Cellular respiration
ATP synthesis coupled electron transport
Generation of precursor metabolites and energy
Astro-WM & Astro-GMii
Regulation of cell differentiation
Regulation of cell motility and migration
Respond to wounding
Astro-GM
Cell projection morphogenesis
Neuron projection development
Modulation of chemical synaptic transmission
Regulation of trans-synaptic signaling
Astro-GM & Astro-GMii
Import into cell
Neurotransmitter uptake
Ion transmembrane transport
Sodium ion transport
Astro-GMii
Cellular response to cytokine
Response to external biotic stimulus
Sterol biosynthetic process
Organic hydroxy compound biosynthetic process
Astro-WM
Astro-GM
Astro-GMii
Ctsh
Hexa
Arpc1b
Gpx4
Trem2
C3
Prdx6
Fcer1g
Ctsd
Cyba
Ctss
C1qa
C1qc
Tyrobp
C1qb
Lyz2
Ctsz
S100a6
Serpina3n
Cd44
Clu
Cd9
Ctsb
H2-D1
B2m
Cd63
C4b
Olfml3
Vegfa
Gpr37l1
Fgfr3
Ccl2
H2-K1
Lgals3bp
Csf1
Ctsl
Fgfr1
Trophic genes
Pro-inflammatory genes
o
Sub-clusters of astrocytes
UMAP-1
UMAP-2
1
2
3
4
5
p
GMii_Score
Cluster
q
Nnat
Gfap
Rbp1
Fabp7
S100a6
Fxyd1
Ptn
Lgals3
Lyz2
Paqr7
Gng11
Ctsd
Cox6a1
Scrg1
Spp1
Mbp
Tssc4
Gm4951
Iigp1
Rsad2
Cxcl10
Igtp
Gbp7
Ifit3
Gbp2
Ccl2
Ccl7
Slc2a1
Vegfa
Sez6l
Malat1
ENSMUSG00000097971
Ndfip1
Pfkp
Bdkrb2
Lars2
Lcn2
Insig1
Idi1
Dcaf17
Ifit1
Cdkn1a
Tiparp
Neat1
Tsc22d3
Usp53
Timp3
Oxidative phosphorylation
NADH dehydrogenase complex assembly
Mitochondrial respiratory chain complex I assembly
Aerobic respiration
Mitochondrial respiratory chain complex assembly
Energy coupled proton transport
ATP synthesis coupled proton transport
Proton transmembrane transport
Electron transport chain
Respiratory electron transport chain
Response to interferon-beta
Cellular response to interferon-beta
Sterol biosynthetic process
Cholesterol biosynthetic process
Secondary alcohol biosynthetic process
Steroid biosynthetic process
Negative regulation of viral process
Cellular response to lipopolysaccharide
Regulation of viral process
Cellular response to molecule of bacterial origin
Import across plasma membrane
Positive regulation of epithelial cell migration
Positive regulation of endothelial migration
Import into cell
Endothelial cell development
Regulation of endothelial cell migration
Regulation of mRNA processing
Regulation of RNA splicing
Regulation of mRNA splicing, via spliceosome
Positive regulation of mRNA metabolic process
Negative regulation of mRNA metabolic process
Alternative mRNA spicing, via spliceosome
Negative regulation of translation
Regulation of alternative mRNA splicing
Regulation of RNA stability
Ribonucleoprotein complex subunit organization
Positive regulation of RNA splicing
Ribonucleoprotein complex assembly
Normalized expression
p. adjust
Count